Atmos. Chem. Phys. Discuss., 8, 20463–20500, 2008
www.atmos-chem-phys-discuss.net/8/20463/2008/

Atmospheric Chemistry and Physics Discussions

This discussion paper is/has been under review for the journal *Atmospheric Chemistry and Physics (ACP)*. Please refer to the corresponding final paper in *ACP* if available.

Global distribution and radiative forcing of soil dust aerosols in the Last Glacial Maximum simulated by the aerosol climate model

T. Takemura[1], M. Egashira[2], K. Matsuzawa[2], H. Ichijo[3], R. O'ishi[3], and A. Abe-Ouchi[3]

[1]Research Institute for Applied Mechanics, Kyushu University, Fukuoka, Japan
[2]Interdisciplinary Graduate School of Engineering Sciences, Kyushu Univ., Fukuoka, Japan
[3]Center for Climate System Research, University of Tokyo, Chiba, Japan

Received: 12 September 2008 – Accepted: 15 October 2008 – Published: 9 December 2008

Correspondence to: T. Takemura (toshi@riam.kyushu-u.ac.jp)

Published by Copernicus Publications on behalf of the European Geosciences Union.

Abstract

The integrated simulation for the global distribution and radiative forcing of soil dust aerosols in the Last Glacial Maximum (LGM) is done by an aerosol climate model, SPRINTARS, in this study. It is compared with another simulation in the present climate condition. The global total emission flux of soil dust aerosols in the LGM is simulated to be about 2.4 times as large as that in the present climate, and the simulated deposition flux is in general agreement with estimations from ice core and marine sediment samplings though it might be underestimated over the Antarctic. The calculated direct radiative forcing of soil dust aerosols in the LGM is close to zero at the tropopause and $-0.4\,\mathrm{W\,m^{-2}}$ at the surface, which are about twice as large as those in the present climate. SPRINTARS also includes the microphysical parameterizations of the cloud-aerosol interaction both for liquid water and ice crystals, which affect the radiation budget. The positive radiative forcing of the indirect effect due to soil dust aerosols, that is mainly caused by a role of ice nuclei, is simulated to be smaller in the LGM than in the present. It is suggested that atmospheric dust might contribute to the cold climate during the glacial periods both through the direct and indirect effects, relative to the interglacial periods.

1 Introduction

The air temperature during the glacial and interglacial periods has been analyzed with ice cores, marine sediments, and pollens. It is assumed that the annual mean surface air temperature is about 3 and 10 K lower in the Last Glacial Maximum (LGM), which is about twenty-one thousands years ago, than in the present climate over the tropics and southern Europe, respectively, and 3 to 6 K lower on the global mean (Jouzel et al., 1993; Kucera et al., 2005; Masson-Delmotte et al., 2005; Wu et al., 2007). It is thought to be impossible to quantitatively explain the remarkable low temperature and extended ice sheets in the LGM only with the change in the insolation. It is a general opinion that

ACPD

8, 20463–20500, 2008

the lower greenhouse gas concentrations, extended ice sheets, and feedback mechanisms within and among the atmosphere, ocean, cryosphere, and vegetation play important roles in the LGM climate. Jansen et al. (2007) reported based on the Paleoclimate Modeling Intercomparison Project 2 (PMIP-2) (Braconnot et al., 2007) that the radiative perturbation in the LGM, which do not include the effects of vegetation and aerosol changes, is estimated to be -4 to $-7\,\mathrm{W\,m^{-2}}$ due to lower greenhouse gas concentrations, extended continental ice, and lower sea level than the present climate, and that the scientific understanding of the radiative perturbation due to atmospheric mineral dust is very low.

From analyses of ice cores and sediments, it has been found that the deposition flux of atmospheric soil dust aerosols varies between the glacial and interglacial periods. Soil dust aerosols are considered as one of the factors inducing climate change principally through two effects. One is the direct effect in which they scatter and absorb the solar and thermal radiation. The other is the indirect effect in which they alter the microphysical and optical properties of cloud droplets and ice crystals acting as cloud condensation nuclei (CCN) and ice nuclei (IN). Soil dust is one of the essential aerosols for IN although it has less effect for CCN because of hydrophobicity in the external mixing with other aerosols. The aerosol semi-direct effect is also discussed, in which aerosols that absorb the solar and/or thermal radiation, such as soil dust, warm the surrounding atmosphere, resulting in changes in the atmospheric stability and cloud production. Therefore the difference in the concentration of soil dust aerosols between the glacial and interglacial periods may contribute to large difference in the climate condition between them. Petit et al. (1999) indicated that the concentration of soil dust aerosols in the ice core from Vostok, Antarctica is order-of-magnitude larger in the glacial than in the interglacial periods, especially in the LGM. The data of marine sediments also show that the dust fluxes from Africa transported to the tropical and subtropical Atlantic in the LGM are three to five times higher than the present-day (Harrison et al., 2001). The increase of the soil dust concentration in the LGM may assign the less precipitation, expansion of land areas, and strong wind.

To simulate and analyze the soil dust emission, concentration, and deposition in the LGM, several modeling studies have proceeded. Joussaume (1993) demonstrated the desert dust cycle in the LGM with an atmospheric general circulation model (AGCM), however only a weak increase was simulated. Andersen et al. (1998) simulated larger dust amounts almost everywhere over the globe in the LGM than in the present-day considering variation of the soil moisture, but they were still lower than values reported from ice cores. They indicated that inclusion of more realistic boundary conditions for the dust emission (e.g., vegetation) could also improve the LGM dust cycle. Mahowald et al. (1999) showed that the simulated dust deposition flux in the LGM were roughly in agreement with observed data from marine sediments and ice cores by including a difference in vegetation between the glacial and interglacial periods. They suggested that changes in source areas are required to predict any substantial increase in the dust deposition over the polar region. Werner et al. (2002) suggest from their simulation that one third of an increase in the total global dust emission flux in the LGM is related to source-region changes, while two thirds is caused by glacial wind speed changes over modern dust emission regions. Mahowald et al. (2006) indicated that the impact of CO_2 fertilization on arid vegetation and the glaciogenic dust sources are sensitive to dust sources. Mentioned above, the previous studies have improved the reproductivity of the atmospheric dust condition in the LGM by the simulations.

Soil dust aerosols affect the radiation budget through the direct and indirect effects as mentioned above, so that they may have important potential to compound the climate system in the glacial period. The PMIP-2, however, did not treat the dust effects on the climate system as well as the coupled ocean-atmosphere system. Claquin et al. (2003) simulated the direct radiative forcing of dust based on Mahowald et al. (1999). In this study, the radiative forcings both of the direct and indirect effects by soil dust aerosols in the LGM are calculated with a global aerosol climate model, Spectral Radiation-Transport Model for Aerosol Species (SPRINTARS), which is accompanied by the simulation of global distributions for main tropospheric aerosols, using the prescribed sea surface temperature (SST) and sea ice by the ocean-atmosphere coupled

ACPD
8, 20463–20500, 2008

general circulation model. One of the significant features of this study is inclusion of the interaction between ice crystals and aerosol particles in order to calculate the aerosol indirect effect. The model description is given in Sect. 2. Section 3 shows the simulated emission, distribution, and deposition of soil dust aerosols as well as sea salt aerosols both in the LGM and present-day. The simulated deposition fluxes of soil dust aerosols are compared with their estimations from ice cores and marine sediments in order to understand reproductivity and problems of the present model. Section 4 presents the calculated direct and indirect radiative forcings of soil dust aerosols and discuss their effects on the climate system in the LGM. This study is concluded in Sect. 5.

2 Model description

In this study, global distributions and radiative forcings of aerosol particles in the LGM climate condition are simulated by SPRINTARS (Takemura et al., 2000, 2002, 2005). It is fully coupled with an AGCM developed by the Center for Climate System Research (CCSR)/University of Tokyo, National Institute for Environmental Studies (NIES), and Frontier Research Center for Global Change (FRCGC) (K-1 Model Developers, 2004). In this study, the horizontal resolution is T42 (approximately 2.8° by 2.8° in latitude and longitude) and the vertical resolution is 20 layers (sigma levels based on the surface pressure at 0.995, 0.980, 0.950, 0.900, 0.830, 0.745, 0.650, 0.549, 0.454, 0.369, 0.295, 0.230, 0.175, 0.124, 0.085, 0.060, 0.045, 0.035, 0.025, and 0.008).

SPRINTARS predicts mass mixing ratios of the main tropospheric aerosols, that is, carbonaceous (black carbon (BC) and organic carbon (OC)), sulfate, soil dust, and sea salt, and the precursor gases of sulfate, that is, sulfur dioxide (SO_2) and dimethylsulfide (DMS). The aerosol transport processes include emission, advection, diffusion, sulfur chemistry, wet deposition, dry deposition, and gravitational settling. The emission flux of soil dust aerosols depends on the near-surface wind speed, vegetation, leaf area index (LAI), soil moisture, and snow amount (see Appendix A). The vegetation and monthly mean LAI distributions are prescribed with the simulation by the

ACPD
8, 20463–20500, 2008

CCSR/NIES/FRCGC AGCM coupled with the Lund-Potsdam-Jena Dynamic Global Vegetation Model (LPJ-DGVM) (Sitch et al., 2003; Gerten et al., 2004). The potential vegetation types for dust emission are wooded c4 grassland, bare ground/shrub, tundra, and warm grassland/shrub in this study (Fig. 1). The bare ground/shrub in the LGM expands over the inland Asia, Middle and Near East, and southern Sahara in comparison with the present condition. The tundra also increases in the LGM, which is partly due to expansion of land because of sea level falling, although there are large-scale ice sheets over the North America and Northern Europe. The prescribed vegetation distribution in the LGM is confirmed to be in general agreement with reconstruction data (Harrison and Prentice, 2003). Figure 2 shows the annual mean LAI distribution, and it is possible to emit soil dust aerosols if the LAI is less than about 0.575 according to Eqs. (A3)–(A4). The other natural emissions included in this study is sea salt aerosols (see Appendix B), BC, OC, and SO_2 from biomass burning, OC from the gas-to-particle conversion of terpene (Guenther et al., 1995), and dimethylsulfide (DMS) from oceanic phytoplankton and land. The global distribution of emission for biomass burning BC is based on the monthly mean data of the Global Fire Emissions Database version 2 (GFEDv2) from the year 1997 to 2006 (Randerson et al., 2005), and the natural sources are assumed to be 10% of the total GFEDv2 emission (Andreae, 1991). The natural emissions of BC and OC mentioned above are assumed to be the same between the simulations for the LGM and a present climate condition. A scheme of the DMS emission from oceanic phytoplankton which is a function of the downward surface solar radiation is the same as Takemura et al. (2000) and that from land vegetation and soil which is function of LAI, solar zenith angle, and temperature is according to Spiro et al. (1992). The other transport processes are according to Takemura et al. (2000, 2002, 2005).

The radiation scheme in the CCSR/NIES/FRCGC AGCM, which adopts the two-stream discrete ordinate and adding method (Nakajima et al., 2000), includes the calculation of the aerosol direct effect. The refractive indices depending on wavelengths, size distributions, and hygroscopic growth are considered for each kind of aerosol. The

ACPD
8, 20463–20500, 2008

refractive indices of dry aerosols and water are according to Deepak and Gerber (1983) and d'Almeida et al. (1991), respectively, except the imaginary part of soil dust aerosols which is a quarter of values in Deepak and Gerber (1983) because their weaker absorption of the solar radiation has been recently reported (e.g., Kaufman et al., 2001). The detailed description of the aerosol direct effect in SPRINTARS is in Takemura et al. (2002, 2005).

The aerosol indirect effect is also included both for water and ice clouds in SPRINTARS. The cloud droplet and ice crystal number concentrations are prognostic variables. The nucleation of the cloud droplets depends not only on the aerosol particle number concentrations but also on the size distributions, curvature effect, and solute effect of each kind of aerosol, and the updraft velocity. The nucleation of the ice crystal number concentration includes both the homogeneous and heterogeneous processes (see Appendix C). The growth and collision processes for cloud droplets and ice crystals are described also in Appendix C. Changes in the cloud droplet and ice crystal number concentrations induce changes in the cloud droplet and ice crystal effective radii, respectively, that is the first indirect effect, which result in a change in the radiation budget. The precipitation rate for warm rain is according to the Berry's parameterization depending on the cloud droplet number concentration, that is the second indirect effect. The detailed description of the aerosol indirect effect for water coluds in SPRINTARS is in Takemura et al. (2005). Note that a change in the precipitation rate for cold rain is not included in the present version of SPRINTARS.

The initial condition and the climatological monthly mean data of SST and sea ice in the LGM are prescribed with the simulated result by the CCSR/NIES/FRCGC atmosphere-ocean coupled general circulation model (AOGCM), MIROC (Model for Interdisciplinary Research on Climate) which is based on PMIP-2 (Yanase and Abe-Ouchi, 2007). The model result shows about 2.5 to 3 K SST change in the low latitude and about 5 K global change, which is in the range of uncertainty of reconstructed data of different proxies and also comparable performance to other coupled AOGCMs in PMIP2 experiments (Masson-Delmotte et al., 2005; Kageyama et al., 2006). As a ref-

ACPD
8, 20463–20500, 2008

erence simulation SPRINTARS also calculates global distributions and radiative forcings of aerosols in the pre-industrial era as a present climate condition (PRE). The HadISST (Rayner et al., 2003) averaged from the year 1870 to 1879 is used as the monthly SST and sea ice in the PRE simulation. The solar radiative flux at the top of the atmosphere is calculated with the eccentricity, obliquity of the earth's axis, and longitude of perihelion (Table 1). The atmospheric CO_2, N_2O, and CH_4 concentration are set to be constant globally and annually (Table 1). Each experiment is integrated for 6 years and analyzed for the last 5 years.

3 Aerosol emission, distribution, and deposition in the LGM

Figure 3a and b shows simulated global distributions of the annual dust emission in the LGM and PRE, respectively. In the PRE, the main emission sources are distributed between 50° N to 40° S; the Sahara, Middle East, Central Asia, Kalahari Desert, Patagonia, and Australia. In the LGM, they expand into south over the Sahara and into north over the Eastern Europe and Central Asia due to extended arid regions (Fig. 1). The other sources appear over the northern Siberia during the glacial period because of the sea level falling. As well as expansion of emission sources, the dust emission flux is also larger over the Sahara, Middle and Near East, Asia, and Europe in the LGM than in the PRE (Table 2). The global total flux in the LGM is calculated to be 6200 Tg/yr, about 2.4 times as large as that in the PRE. Werner et al. (2002) estimated 2.2-fold higher dust emission flux in the LGM, which is close to this study, though their estimation of the total flux was smaller (2383 Tg/yr). The dust emission flux under the present climate condition was estimated to be 2594 Tg/yr in this study, which is in agreement with most past studies, ranging about from 1500 to 3000 Tg/yr (e.g., Tegen and Fung, 1994; Dentener et al., 1996; Chin et al., 2002; Tanaka and Chiba, 2005), while Werner et al. (2002) estimated it to be 1060 Tg/yr.

Reasons for the high dust emission flux in the LGM are assumed to be mainly due to not only expansion of emission sources but also strong wind in the LGM. In order to

ACPD
8, 20463–20500, 2008

separate the influence of extended arid regions from the other meteorological factors on the dust emission flux, an additional experiment (LGMfv) is done with the present-day vegetation distribution as shown in Fig. 1b and with the same conditions as LGM for others. Table 2 shows that the large emission flux of soil dust aerosols in the LGM is more affected by the meteorological condition than the vegetation over the Sahara and Middle and Near East, and vice versa over Asia and Europe. The simulation suggests that about 60% of the increase in the global total dust emission in the LGM relative to PRE is due to a difference in the meteorological condition, especially the strong wind, and the other is due to a difference in vegetation. These rations of contributing to an increase in the LGM dust emission are close to those in Werner et al. (2002).

Figure 3c and d shows simulated global distributions of the annual dust column loading in the LGM and PRE, respectively, and Table 3 shows zonal column loading and deposition flux of soil dust aerosols. Those emitted from the Sahara are transported to west by the trade winds and from Asia to east by the westerlies. The atmospheric dust loading is larger in the LGM than in the present all over the Northern Hemisphere, especially in the high latitudes mainly due to expansion of the emission sources. The distribution of the dust deposition flux is similar to that of the mass column loading (not shown). The zonal mean mass column loading and deposition flux in the LGM are about 7 and 20 times, respectively, as large as those in the present between 90° N and 60° N, and 2 to 3 times between 60° N to 0°. The ratio of the dry deposition to the total deposition flux is high near the source regions, and the wet deposition becomes a predominant deposition process with being away from the sources. One of the simulated characteristics in the LGM is a high ratio of the dry deposition in the high latitudes of the Northern Hemisphere. Ratio of the dry deposition is also larger in the LGM in the low- and mid-latitude of the Northern Hemisphere than in the PRE because of the drier atmospheric condition in the LGM as well as the larger mass column loading.

The simulated dust deposition fluxes both in the LGM and PRE are compared with DIRTMAP (Dust Indicators and Records of Terrestrial and Marine Palaeoenvironments) database (Kohfeld and Harrison, 2001) which is estimated mainly from ice cores and

ACPD
8, 20463–20500, 2008

marine sediments. It is best database for understand the simulated results, though there are some uncertainty factors, for example, that the fluxes from ice cores rely on estimates of ice accumulation rate in the cores and that ocean currents can advect dust substantially before it is deposited (Kohfeld and Harrison, 2001; Mahowald et al., 2006). It has been suggested from DIRTMAP that the dust deposition fluxes during the LGM are 2 to 5 times as large as those during interglacial periods in the tropical and mid-latitudes, and over 20 times in the polar regions. Figure 4 shows comparisons of the annual dust deposition fluxes between DIRTMAP and the simulation by SPRINTARS in the LGM and PRE. They are in general agreement in the PRE, though there is a little underestimation over the Indian Ocean. Also in the LGM, the simulation generally captures the five order of magnitude range in the deposition fluxes except the Antarctic region. The isotopic measurement has suggested that the ice-core dust in the Antarctic during glacial periods have a primary origin from Patagonia with a small amount (10 to 15%) from southern Africa and/or Australia (Basile et al., 1997). There are three possible reasons for underestimating the dust emission from Patagonia in the LGM simulated in this study as shown in Fig. 3 and Table 2. The first is inappropriate vegetation indices and underestimation of emerging land due to the sea level falling because there is a large difference in the emission flux from the South America between the LGM and LGMfv. The second is underestimation of wind speed because the emission flux in the LGMfv experiment is smaller than in the PRE, in spite of vice versa in the Northern Hemisphere. The other additional reason is underestimation of precipitation, because the deposition flux over the high latitudes of the Southern Hemisphere in the LGM is a half of that in the present though the mass column loading in the LGM is a little larger than that in the present and because the wet deposition is a primary process in the total dust deposition (Table 3).

The other principal natural aerosol is sea salt. Figure 5 shows simulated distributions of the annual emission flux and annual mean mass column loading of sea salt aerosols, and Table 4 presents their zonal and global total emission fluxes in the LGM and PRE. Both the emission flux and atmospheric loading in the LGM is similar to those in the

present in the tropics and mid-latitudes, though the emission flux in the LGM is slightly larger due to the stronger wind. On the other hand, the emission is prevented by extended sea ice in the LGM in the high latitudes. This study cannot analyze differences in natural carbonaceous and sulfate aerosols between the LGM and PRE because their setup is almost same both in the simulations.

4 Dust radiative forcing in the LGM

The direct radiative forcing of soil dust aerosols is calculated as a difference in the radiative budget between inclusion and exclusion of soil dust aerosol in the radiative process within one simulation. Figure 6 shows the annual mean distributions of the direct radiative forcing due to soil dust aerosols under the all-sky condition. The forcing at the tropopause is basically negative over oceanic and forest areas, while it is positive over arid regions due to high surface albedo. Even over the ocean where the surface albedo is low, it is partly positive, in spite of small values, because soil dust aerosols multiply absorb scattered solar radiation enhanced by the lower cloud layer than the aerosol layer. It has been known that the aerosol direct radiative forcing at the tropopause and top of the atmosphere is much sensitive to the vertical structure of cloud layers for aerosol species absorbing the solar radiation (Haywood and Ramaswamy, 1998; Takemura et al., 2002). A significant characteristic in the LGM is the strong positive forcing over the northern Europe and Arctic Ocean due to extended and continuous ice sheets and sea ice through the year. At the surface, the direct radiative forcing is negative almost over the globe because the solar radiation is attenuated at the surface whether soil dust aerosols scatter or absorb it. The negative forcing is generally in correspondence to the column loading (Fig. 3c and d) and larger in the LGM than in the present.

Table 5 shows the annual global mean direct forcing both under the clear-sky and all-sky conditions. The negative shortwave forcing and positive longwave forcing under the all-sky condition are smaller than the clear-sky due to absorbing the multi-scattered

ACPD
8, 20463–20500, 2008

radiation with lower cloud layer as mentioned above and due to absorption of the terrestrial radiation by clouds, respectively. A difference in the global mean direct forcing between the LGM and PRE both in the shortwave and longwave radiation is approximately proportional to a difference in the emission flux and column loading (Tables 2 and 3). In the LGM, the direct radiative forcing of soil dust aerosols is close to zero at the tropopause and $-0.4\,\mathrm{W\,m^{-2}}$ at the surface.

The indirect radiative forcing of soil dust aerosols in the LGM is also estimated in this study. Soil dust aerosols play an important role as ice nuclei in forming ice crystals through the heterogeneous nucleation (Lohmann and Feichter, 2005), though they are not much effective in forming water cloud droplets. Appendix C shows the microphysical treatment for the relationship between ice crystals and aerosol particles in the model. The indirect radiative forcing is calculated as a difference in the cloud radiative forcing between inclusion and exclusion of the dust emission. Figure 7 shows the annual mean distribution of the indirect radiative forcing due to soil dust aerosols both in the LGM and PRE. Inclusion of soil dust aerosol as ice nuclei results in smaller ice crystals, which leads to absorption of the longwave radiation more effectively than scattering of the shortwave radiation. Therefore the indirect forcing is positive at the tropopause almost over the globe. At the surface, on the other hand, attenuation of the shortwave radiation due to the smaller ice crystals is prominent. The indirect radiative forcing is large where the ice water content is large. The obvious difference between the LGM and PRE is the large positive forcing at the tropopause and the large negative forcing at the surface in the PRE, especially over the tropics because of the reduced ice crystal concentration due to inactive convection in the LGM.

The global mean indirect forcing is larger in the PRE at the tropopause both in the negative shortwave and positive longwave radiations than in the LGM though the dust loading is larger in the LGM (Table 6). It might be because the ice and liquid water contents are generally less in the LGM due to the low temperature. The simulated ice water path on the global mean in the LGM is 11% less than that in the present. The global mean positive value of the net indirect radiative forcing due to soil dust aerosols

ACPD
8, 20463–20500, 2008

in the LGM (+2.0 W m^{-2}) is smaller than that in the PRE (+2.9 W m^{-2}), therefore atmospheric dust might contribute to the cold climate during the glacial periods through the indirect effect as well as the direct effect relative to the interglacial periods.

5 Conclusions

Global dust distribution and radiative forcings both of the direct and indirect effect in the LGM were simulated by the global aerosol climate model, SPRINTARS, in this study. The global total dust flux in the LGM is calculated to be about 2.4 times as large as that in the present climate mainly because of the extended arid regions and strong wind. The simulated dust deposition flux was in general agreement with estimations from ice core and marine sediment samplings. Further studies are, however, needed to solve underestimation of the simulated dust deposition over the Antarctic through, for example, detailed sensitivity experiments for analyzing what important factors are to determine the emission, atmospheric loading, and deposition of soil dust aerosols. The global mean negative value of the direct radiative forcing due to soil dust aerosols at the tropopause in the LGM was simulated to be larger than that in the present climate, and the positive value of the indirect effect in the LGM was smaller. Therefore this study suggested that they contribute to the lower temperature during the glacial periods relative to the interglacial periods.

The detailed and progressive studies with atmosphere-ocean coupled general circulation models or earth system models will be important to quantitatively analyze the effects of atmospheric dust on the climate system including feedback processes in the glacial periods. To understand the climate in the glacial period when it is extremely different in the present are closely related to analyze the essential climate formation and the modern climate change.

ACPD
8, 20463–20500, 2008

Appendix A

Emission flux of soil dust aerosols

A scheme of the emission mass flux of soil dust aerosols F_{ed} in this study has been improved from the previous version of SPRINTARS (Takemura et al., 2000):

$$F_{ed} = \begin{cases} A_e C \left(|\boldsymbol{v}_{10}| - u_t\right) |\boldsymbol{v}_{10}|^2 & \text{for } |\boldsymbol{v}_{10}| \geq u_t \\ 0 & \text{for } |\boldsymbol{v}_{10}| < u_t \end{cases}, \tag{A1}$$

where $|\boldsymbol{v}_{10}|$ is the wind speed at 10-m height, u_t is the threshold velocity set to be $6.5\,\mathrm{m\,s^{-1}}$, C is the emission coefficient depending on the soil moisture W_g, snow amount W_s, and region defined as,

$$C = \begin{cases} C_d \frac{W_{gt} - W_g}{W_{gt}} & \text{for } W_g \leq W_{gt} \text{ and } W_s \leq W_{st} \\ 0 & \text{for others} \end{cases}, \tag{A2}$$

where C_d, W_{gt} are the coefficient and threshold soil moisture depending on the region and W_{st} is the threshold snow amount, and A_e is the effective area in emitting soil dust aerosols according to Tegen et al. (2002):

$$A_e = \begin{cases} 1 - \mathrm{FPAR} & \text{for FPAR} \leq 0.25 \\ 0 & \text{for FPAR} > 0.25 \end{cases}, \tag{A3}$$

$$\mathrm{FPAR} = 1 - \exp\left(-0.5 \times \mathrm{LAI}\right), \tag{A4}$$

where FPAR is the fraction absorbed photosynthetically active radiation. SPRINTARS predicts the mass mixing ratio of soil dust aerosols dividing radii into 6 bins from 0.1 to 10 µm. Table 1 shows the normalized emission strength of each size bin based on d'Almeida and Schütz (1983).

ACPD
8, 20463–20500, 2008

Appendix B

Emission flux of sea salt aerosols

A scheme of the emission mass flux of sea salt aerosols F_{es} in this study has been changed from the previous version of SPRINTARS (Takemura et al., 2000). The new scheme is based on Monahan et al. (1986):

$$\frac{dF_{es}}{dr} = \frac{4}{3}\pi\rho_s a |\boldsymbol{v}_{10}|^b r^{-3}\left(1 + cr^d\right) \times 10^{f\exp\left[-\{(g-\log r)/h\}^2\right]}, \quad \text{(B1)}$$

where r and ρ_s are the radius and density of sea salt aerosol, respectively, and a, b, c, d, f, g, and h are constants according to Monahan et al. (1986). SPRINTARS predicts the mass mixing ratio of sea salt aerosols dividing radii into 4 bins from 0.1 to 10 µm (Table 1).

Appendix C

Parameterization of interaction between aerosols and ice crystals

The latest version of SPRINTARS treats the cloud droplet number concentration n_l and ice crystal number concentration n_i as prognostic variables:

$$\frac{\partial n_l}{\partial t} = R(n_l) + N_{nuc} - N_{sel} - N_{frc} - N_{fri} - \frac{n_l}{q_l}\left(Q_{aut} + Q_{arl} + Q_{asl}\right), \quad \text{(C1)}$$

$$\frac{\partial n_i}{\partial t} = R(n_i) + N_{frh} + N_{frc} + N_{fri} - N_{agg} - \frac{n_i}{q_i}Q_{asi}, \quad \text{(C2)}$$

where R indicates the advection and diffusion terms, q_l and q_i are the in-cloud mass mixing ratios of cloud water and ice, respectively, and the time-varying terms N and Q with subscripts are as follows: N_{nuc} is the nucleation of cloud droplets, N_{frh} is the

ACPD
8, 20463–20500, 2008

homogeneous freezing of supercooled aerosols, N_{frc} is the contact freezing, N_{fri} is the immersion/condensation freezing, N_{sel} is the self-collection of cloud droplets, N_{agg} is the aggregation of ice crystals, Q_{aut} is the autoconversion of cloud droplets, Q_{arl} and Q_{asl} are the accretion of cloud droplets by rain and snow, respectively, and Q_{asi} is the accretion of ice crystals by snow. The nucleation of cloud droplets N_{nuc} is according to Eqs. (1)–(4) in Takemura et al. (2005). The homogeneous freezing N_{frh} is based on Kärcher and Lohmann (2002). BC and soil dust aerosols act as IN for the heterogeneous freezing including the contact and immersion/condensation processes. Ratios of activated IN to the total number concentration of BC and dust for the contact freezing f_{frc} and the immersion/condensation freezing f_{fri} are based on Fig. 1 in Lohmann and Diehl (2006):

$$f_{frc} = a_c\,(273.15 - T) - b_c\,, \tag{C3}$$

$$f_{fri} = \begin{cases} \exp\left\{-\left(\frac{T_{i0}-T}{T_i}\right)^2\right\} & \text{for } T \geq T_{i0} \\ 1 & \text{for } T < T_{i0} \end{cases}, \tag{C4}$$

where T is the temperature in K, a_c, b_c, T_{i0} are constants depending on aerosol species (Table 1), and $T_i = 3$ K. The terms of N_{frc} and N_{fri} are according to Lohmann and Diehl (2006) and Diehl et al. (2006). The deposition freezing is neglected in this study because it generally takes place at lower temperatures and higher supersaturation than the other heterogeneous freezing processes (Lohmann and Diehl, 2006). The self-collection of cloud droplets N_{sel} and the aggregation of ice crystals N_{agg} are following Lohmann et al. (1999) and Levkov et al. (1992), respectively. The Berry's parameterization (Berry, 1967) is adopted as the autoconversion of cloud droplets Q_{aut} (Eq. (6) in Takemura et al., 2005). The accretion of cloud droplets by rain and snow is calculated as:

$$Q_{arl,asl} = F_p E_l q_l\,, \tag{C5}$$

ACPD
8, 20463–20500, 2008

where F_p is the in-cloud flux of rain or snow and E_l is a constant, 1.0 for rain and 0.5 by snow. The accretion of ice crystals by snow is also calculated as:

$$Q_{asi} = F_p E_i q_i, \quad \text{(C6)}$$

where E_i is 0.05.

Acknowledgements. We would like to thank the contributors of development of SPRINTARS and MIROC, DIRTMAP investigators, and anonymous reviewers. The simulation in this study was performed by the NIES supercomputer system (NEC SX-8R). This study is supported by the Grant-in-Aid for Young Scientists of the Ministry of Education, Culture, Sports, Science, and Technology of Japan.

References

Andersen, K. K., Armengaud, A., and Genthon, C.: Atmospheric dust under glacial and interglacial conditions, Geophys. Res. Lett., 25, 2281–2284, 1998. 20466

Andreae, M. O.: Biomass burning: Its history, use, and distribution and its impact on environmental quality and global climate, in: Global Biomass Burning: Atmospheric, Climatic, and Biospheric Implications, edited by: Levine, J. S., MIT Press, Cambridge, Mass., USA, 3–21, 1991. 20468

Basile, I., Grousset, F. E., Revel, M., Petit, J. R., Biscaye, P. E., and Barkov, N. I.: Patagonian origin of glacial dust deposited in East Antarctica (Vostok and Dome C) during glacial stages 2, 4 and 6, Earth Planet. Sc. Lett., 146, 573–589, 1997. 20472

Berry, E. X.: Cloud droplet growth by collection, J. Atmos. Sci., 24, 688–701, 1967. 20478

Braconnot, P., Otto-Bliesner, B., Harrison, S., Joussaume, S., Peterchmitt, J.-Y., Abe-Ouchi, A., Crucix, M., Driesschaert, E., Fichefet, Th., Hewitt, C. D., Kageyama, M., Kitoh, A., Laîné, A., Loutre, M.-F., Marti, O., Merkel, U., Ramstein, G., Valdes, P., Weber, S. L., Yu, Y., and Zhao, Y.: Results of PMIP2 coupled simulations of the Mid-Holocene and Last Glacial Maximum – Part 1: experiments and large-scale features, Clim. Past, 3, 261–277, 2007, http://www.clim-past.net/3/261/2007/. 20465

Chin, M., Ginoux, P., Kinne, S., Torres, O., Holben, B. N., Duncan, B. N., Martin, R. V., Logan, J. A., Higurashi, A., and Nakajima, T.: Tropospheric aerosol optical thickness from the GO-

CART model and comparisons with satellite and sun photometer measurements, J. Atmos. Sci., 59, 461–483, 2002. 20470

Claquin, T., Roelandt, C., Kohfeld, K. E., Harrison, S. P., Tegen, I., Prentice, I. C., Balkanski, Y., Bergametti, G., Hansson, M., Mahowald, N., Rodhe, H., and Schulz, M.: Radiative forcing of climate by ice-age atmospheric dust, Clim. Dynam., 20, 193–202, 2003. 20466

d'Almeida, G. A. and Schütz, L.: Number, mass and volume distributions of mineral aerosol and soils of the Sahara, J. Clim. Appl. Meteorol., 22, 233–243, 1983. 20476

d'Almeida, G. A., Koepke, P., and Shettle, E.: Atmospheric Aerosols: Global Climatology and Radiative Forcing, A. Deepak, Hampton, Va., USA, 561 pp., 1991. 20469

Deepak, A. and Gerber, H. G. (Eds.): Report of the experts meeting on aerosols and their climatic effects, World Meteorological Organization, Geneva, Switzerland, Rep. WCP-55, 107 pp., 1983. 20469

Dentener, F. J., Carmichael, G. R., Zhnag, Y., Lelieveld, J., and Crutzen, P. J.: Role of mineral aerosol as a reactive surface in the global troposphere, J. Geophys. Res., 101, 22 869–22 889, 1996. 20470

Diehl, K., Simmel, M., and Wurzler, S.: Numerical sensitivity studies on the impact of aerosol properties and drop freezing modes on the glaciation, microphysics, and dynamics of clouds, J. Geophys. Res., 111, D07202, doi:10.1029/2005JD005884, 2006. 20478

Gerten D., Schaphoff, S., Haberlandt, U., Lucht, W., and Sitch, S: Terrestrial vegetation and water balance: Hydrological evaluation of a dynamic global vegetation model, J. Hydrol., 286, 249–270, 2004. 20468

Guenther, A., Hewitt, C. N., Erickson, D., Fall, R., Geron, C., Graedel, T., Harley, P., Klinger, L., Lerdau, M., McKay, W. A., Pierce, T., Scholes, B., Steinbrecher, R., Tallamraju, R., Taylor, J., and Zimmerman, P.: A global model of natural volatile organic compound emissions, J. Geophys. Res., 100, 8873–8892, 1995. 20468

Harrison, S. P., Kohfeld, K. E., Roelandt, C., and Claquin, T.: The role of dust in climate changes today, at the last glacial maximum and in the future, Earth-Sci. Rev., 54, 43–80, 2001. 20465

Harrison, S. P. and Prentice, I. C.: Climate and CO_2 controls on global vegetation distribution at the last glacial maximum: analysis based on palaeovegetation data, biome modelling and palaeoclimate simulations, Global Change Biol. 9, 983–1004, 2003. 20468

Haywood, J. M. and Ramaswamy, V.: Global sensitivity studies of the direct radiative forcing due to anthrpogenic sulfate and black carbon aerosols, J. Geophys. Res., 103, 6043–6058, 1998. 20473

Jansen, E., Overpeck, J., Briffa, K. R., Duplessy, J.-C., Joos, F., Masson-Delmotte, V., Olago, D., Otto-Bliesner, B., Peltier, W. R., Rahmstorf, S., Ramesh, R., Raynaud, D., Rind, D., Solomina, O., Villalba, R., and Zhang, D.: Palaeoclimate, in: Climate Change 2007: The Physical Science Basis, Contribution of Working Group I to the Fourth Assessment Report of the Intergovernmental Panel on Climate Change, edited by: Solomon, S., Qin, D., Manning, M., Chen, Z., Marquis, M., Averyt, K. B., Tignor, M., and Miller, H. L., Cambridge University Press, Cambridge, UK and New York, NY, USA, 2007. 20465

Joussaume, S.: Paleoclimatic tracers: An investigation using an atmospheric general circulation model under ice age conditions 1. Desert dust, J. Geophys. Res., 98, 2767–2805, 1993. 20466

Jouzel, J., Barkov, N. I., Barnola, J. M., Bender, M., Chappellaz, J., Genthon, C., Kotlyakov, V. M., Lipenkov, V., Lorius, C., Petit, J. R., Raynaud, D., Raisbeck, G., Ritz, C., Sowers, T., Stievenard, M., Yiou, F., and Yiou, P.: Extending the Vostok ice-core record of palaeoclimate to the penultimate glacial period, Nature, 364, 407–412, 1993. 20464

K-1 Model Developers: K-1 coupled GCM (MIROC) description, edited by: Hasumi, H., and Emori, S., K-1 Tech. Rep. 1, 34 pp., Center for Climate System Research, University of Tokyo, Tokyo, Japan, 2004. 20467

Kageyama, M., Laine, A., Abe-Ouchi, A., Braconnot, P., Cortijo, E., Crucifix, M., de Vernal, A., Guiot, J., Hewitt, C. D., Kitoh, A., Kucera, A., Marti, O., Ohgaito, R., Otto-Bliesner, B., Peltier, W. R., Rosell-Melé, A., Vettoretti, G., Weber, S. L., Yu, Y., and MARGO Project Members: Last Glacial Maximum temperatures over the North Atlantic, Europe and Western Siberia: A comparison between PMIP models, MARGO sea-surface temperatures and pollen-based reconstructions, Quaternary Sci. Rev., 25, 2082–2102, 2006. 20469

Kärcher, B. and Lohmann, U.: A parameterization of cirrus cloud formation: Homogeneous freezing of supercooled aerosols, J. Geophys. Res., 107, 4010, doi:10.1029/2001JD000470, 2002. 20478

Kaufman, Y. J., Tanré, D., Dobovik, O., Karnieli, A., and Remer, L. A.: Absorption of sunlight by dust as inferred from satellite and ground-based remote sensing, Geophys. Res. Lett., 28, 1479–1482, 2001. 20469

Kohfeld, K. E. and Harrison, S.: DIRTMAP: The geological record of dust, Earth Sci. Rev., 54, 81–114, 2001. 20471, 20472

Kucera, M., Rosell-Melé, A., Schneider, R., Waelbroeck, C., and Weinelt, M.: Multiproxy approach for the reconstruction of the glacial ocean surface (MARGO), Quaternary Sci. Rev.,

24, 813–819, 2005. 20464
Levkov, L., Rockel, B., Kapitza, H., and Raschke, E.: 3D mesoscale numerical studies of cirrus and stratus clouds by their time and space evolution, Beitr. Phys. Atmos., 65, 35–58, 1992. 20478
Lohmann, U., Feichter, J., Chuang, C. C., and Penner, J. E.: Prediction of the number of cloud droplets in the ECHAM GCM, J. Geophys. Res., 104, 9169–9198, 1999. 20478
Lohmann, U., and Feichter, J.: Global indirect aerosol effects: a review, Atmos. Chem. Phys., 5, 715–737, 2005, http://www.atmos-chem-phys.net/5/715/2005/. 20474
Lohmann, U., and Diehl, K.: Sensitivity studies of the importance of dust ice nuclei for the indirect aerosol effect on stratiform mixed-phase clouds, J. Atmos. Sci., 63, 968–982, 2006. 20478
Mahowald, N., Kohfeld, K., Hansson, M., Balkanski, Y., Harrison, S. P., Prentice, I. C., Schulz, M., and Rodhe, H.: Dust sources and deposition during the last glacial maximum and current climate: A comparison of model results with paleodata from ice cores and marine sediments, J. Geophys. Res., 104, 15 895–15 916, 1999. 20466
Mahowald, N. M., Muhs, D. R., Levis, S., Rasch, P. J., Yoshioka, M., Zender, C. S., and Luo, C.: Change in atmospheric mineral aerosols in response to climate: Last glacial period, preindustrial, modern, and doubled carbon dioxide climates, J. Geophys. Res., 111, D10202, doi:10.1029/2005JD006653, 2006. 20466, 20472
Masson-Delmotte, V., Kageyama, M., Braconnot, P., Charbit, S., Krinner, G., Ritz, C., Guilyardi, E., Jouzel, J., Abe-Ouchi, A., Crucix, M., Gladstone, R. M., Hewitt, C. D., Kitoh, A., LeGrande, A. N., Marti, O., Merkel, U., Motoi, T., Ohgaito, R., Otto-Bliesner, B., Peltier, W. R., Ross, I., Valdes, P. J., Vettoretti, G., Weber, S. L., Wolk, F., Yu, Y.: Past and future polar amplication of climate change: climate model intercomparisons and ice-core constraints, Clim. Dynam., 26, 513–529, doi:10.1007/s00382-005-0081-9, 2005. 20464, 20469
Monahan, E. C., Spiel, D. E., and Davidson, K. L.: A model of marine aerosol generation via whitecaps and wave disruption, in: Oceanic Whitecaps, edited by: Monahan, E. and Niocaill, G. M., D. Reidel, Norwell, Mass., USA, 167–174, 1986. 20477
Nakajima, T., Tsukamoto, M., Tsushima, Y., Numaguti, A., and Kimura, T.: Modeling of the radiative process in an atmospheric general circulation model, Appl. Optics, 39, 4869–4878, 2000. 20468
Randerson, J. T., van der Werf, G. R., Collatz, G. J., Giglio, L., Still, C. J., Kasibhatla, P., Miller,

J. B., White, J. W. C., DeFries, R. S., and Kasischke, E. S.: Fire emissions from C3 and C4 vegetation and their influence on interannual variability of atmospheric CO_2 and d13CO_2, Global Biogeochem. Cy., 19, GB2019, doi:10.1029/2004GB002366, 2005. 20468

Rayner, N. A., Parker, D. E., Horton, E. B., Folland, C. K., Alexander, L. V., Rowell, D. P., Kent, E. C., and Kaplan, A.: Global analysis of sea surface temperature, sea ice, and night marine air temperature since the late nineteenth century, J. Geophys. Res., 108, 4407, doi:10.1029/2002JD002670, 2003. 20470

Petit, J. R., Jouzel, J., Raynaud, D., Barkov, N. I., Barnola, J.-M., Basile, I., Bender, M., Chappellaz, J., Davis, M., Delaygue, G., Delmotte, M., Kotlyakov, V. M., Legrand, M., Lipenkov, V. Y., Lorius, C., Pépin, L., Rits, C., Saltzman, E., and Stievenard, M.: Climate and atmospheric history of the past 420,000 years from the Vostok ice core, Antarctica, Nature, 399, 429–436, 1999. 20465

Sitch, S., Smith, B., Prentice, I. C., Arneth, A., Bondeau, A., Cramer, W., Kaplan, J., Levis, S., Lucht, W., Sykes, M., Thonicke, K., and Venevsky, S.: Evaluation of ecosystem dynamics, plant geography and terrestrial carbon cycling in the LPJ Dynamic Vegetation Model, Global Change Biol., 9, 161–185, 2003. 20468

Spiro, P. A., Jacob, D. J., and Logan, J. A.: Global inventory of sulfur emissions with 1° × 1° resolution, J. Geophys. Res., 97, 6023–6036, 1992. 20468

Takemura, T., Okamoto, H., Maruyama, Y., Numaguti, A., Higurashi, A., and Nakajima, T.: Global three-dimensional simulation of aerosol optical thickness distribution of various origins, J. Geophys. Res., 105, 17 853–17 873, 2000. 20467, 20468, 20476, 20477

Takemura, T., Nakajima, T., Dubovik, O., Holben, B. N., and Kinne, S.: Single-scattering albedo and radiative forcing of various aerosol species with a global three-dimensional model, J. Climate, 15, 333–352, 2002. 20467, 20468, 20469, 20473

Takemura, T., Nozawa, T., Emori, S., Nakajima, T. Y., and Nakajima, T.: Simulation of climate response to aerosol direct and indirect effects with aerosol transport-radiation model, J. Geophys. Res., 110, D02202, doi:10.1029/2004JD005029, 2005. 20467, 20468, 20469, 20478

Tanaka, T. and Chiba, M.: Global simulation of dust aerosol with a chemical transport model, MASINGAR, J. Meteorol. Soc. Japan, 83A, 255–278, 2005. 20470

Tegen, I. and Fung, I.: Modeling of mineral dust in the atmosphere: Sources, transport, and optical thickness, J. Geophys. Res., 99, 22 897–22 914, 1994. 20470

Tegen, I., Harrison, S. P., Kohfeld, K., Prentice, I. C., Coe, M., and Heimann, M.: Impact of vegetation and preferential source areas on global dust aerosol: Results from a model study,

J. Geophys. Res., 107, 4576, doi:10.1029/2001JD000963, 2002. 20476
Werner, M., Tegen, I., Harrison, S. P., Kohfeld, K. E., Prentice, I. C., Balkanski, Y., Rodhe, H., and Roelandt, C.: Seasonal and interannual variability of the mineral dust cycle under present and glacial climate conditions, J. Geophys. Res., 107, 4744, doi:10.1029/2002JD002365, 2002. 20466, 20470, 20471
Wu, H., Guiot, J., Brewer, S., and Guo, Z.: Climatic changes in Eurasia and Africa at the last glacial maximum and mid-Holocene: reconstruction from pollen data using inverse vegetation modelling, Clim. Dynam., 29, 211–229, 2007. 20464
Yanase, W. and Abe-Ouchi, A.: The LGM surface climate and atmospheric circulation over East Asia and the North Pacic in the PMIP2 coupled model simulations, Clim. Past, 3, 439–451, 2007,
http://www.clim-past.net/3/439/2007/. 20469

Table 1. Earth's planetary constants and main greenhouse gas concentrations in the LGM and PRE.

	LGM	PRE
Eccentricity	0.018994	0.016720
Obliquity of the earth's axis, degrees	22.949	23.450
Longitude of perihelion, degrees	114.42	102.04
CO_2, ppm	185	287.96
N_2O, ppb	200	281.30
CH_4, ppb	350	902.48

ACPD
8, 20463–20500, 2008

Table 2. Regional and global total annual emission fluxes of soil dust aerosols in the LGM, PRE, and LGMfv and their ratio of LGM to PRE.

Region	LGM, Tg/yr	PRE, Tg/yr	LGM/PRE	LGMfv, Tg/yr
Sahara	4200	1692	2.48	3629
Middle and Near East	734	447	1.64	698
Asia and Europe	1187	273	4.36	311
Australia	48	83	0.58	91
North America	1.6	3.8	0.41	1.4
South America	16	48	0.33	44
Southern Africa	12	48	0.26	16
Total	6200	2594	2.39	4790

ACPD
8, 20463–20500, 2008

Table 3. Zonal and global total mass column loading and deposition fluxes of soil dust aerosols in the LGM and PRE and their ratio of LGM to PRE. Numbers in parentheses in the deposition fluxes are percentages of the wet deposition fluxes to the total ones.

	Mass column loading			Deposition		
Latitude	LGM, Tg	PRE, Tg	LGM/PRE	LGM, Tg/yr	PRE, Tg/yr	LGM/PRE
90° N–60° N	0.77	0.11	6.80	143 (38%)	6.5 (93%)	21.9
60° N–30° N	6.90	2.69	2.57	1586 (23%)	536 (32%)	2.96
30° N–0°	21.47	9.35	2.29	4345 (13%)	1858 (15%)	2.34
0°–30° S	1.49	1.13	1.32	110 (28%)	156 (16%)	0.71
30° S–60° S	0.18	0.29	0.62	15 (65%)	37 (57%)	0.41
60° S–90° S	0.02	0.02	1.20	0.2 (95%)	0.4 (96%)	0.50
Total	30.84	13.60	2.27	6200 (17%)	2594 (19%)	2.39

ACPD
8, 20463–20500, 2008

Table 4. Zonal and global total annual emission fluxes of sea salt aerosols in the LGM and PRE, and their ratio of LGM to PRE.

Latitude	LGM, Tg/yr	PRE, Tg/yr	LGM/PRE
90° N–60° N	21	76	0.27
60° N–30° N	638	697	0.91
30° N–0°	502	488	1.03
0°–30° S	554	539	1.03
30° S–60° S	1693	1963	0.86
60° S–90° N	26	191	0.14
Total	3433	3955	0.87

Table 5. Global and annual mean radiative forcing for the direct effect of soil dust aerosols at the tropopause and surface under clear-sky and all-sky conditions in the LGM and PRE. SW, LW, and SW+LW are shortwave, longwave, and shortwave plus longwave radiations, respectively.

	Tropopause, W m^{-2}			Surface, W m^{-2}		
	SW	LW	SW+LW	SW	LW	SW+LW
Clear-sky						
LGM	−0.38	+0.26	−0.12	−1.02	+0.53	−0.50
PRE	−0.18	+0.11	−0.07	−0.46	+0.22	−0.24
All-sky						
LGM	−0.24	+0.22	−0.02	−0.88	+0.45	−0.43
PRE	−0.10	+0.09	−0.01	−0.38	+0.18	−0.20

ACPD
8, 20463–20500, 2008

Table 6. Global and annual mean radiative forcing for the indirect effect of soil dust aerosols at the tropopause and surface in the LGM and PRE. SW, LW, and SW+LW are shortwave, longwave, and shortwave plus longwave radiations, respectively.

	Tropopause, W m^{-2}			Surface, W m^{-2}		
	SW	LW	SW+LW	SW	LW	SW+LW
LGM	−2.81	+4.83	+2.02	−2.42	+1.25	−1.17
PRE	−3.91	+6.79	+2.88	−3.08	+1.03	−2.05

ACPD
8, 20463–20500, 2008

Table A1. Radius range, effective radius, and normalized emission strength of each size bin for soil dust aerosols in SPRINTARS.

Radius range, μm	Effective radius, μm	Normalized emission strength
0.10–0.22	0.13	0.0045
0.22–0.46	0.33	0.0290
0.46–1.00	0.82	0.1766
1.00–2.15	1.27	0.2633
2.15–4.64	3.20	0.2633
4.64–10.00	8.02	0.2633

Table B1. Radius range and effective radius of each size bin for sea salt aerosols in SPRINTARS.

Radius range, μm	Effective radius, μm
0.100–0.316	0.178
0.316–1.000	0.562
1.000–3.160	1.780
3.160–10.000	5.620

ACPD
8, 20463–20500, 2008

Table C1. Constants for Eqs. (C3) and (C4).

Aerosol	a_c, K^{-1}	b_c	T_{i0}, K
dust	0.1014	0.3277	241.15
BC	0.00978	0.0913	232.15

ACPD
8, 20463–20500, 2008

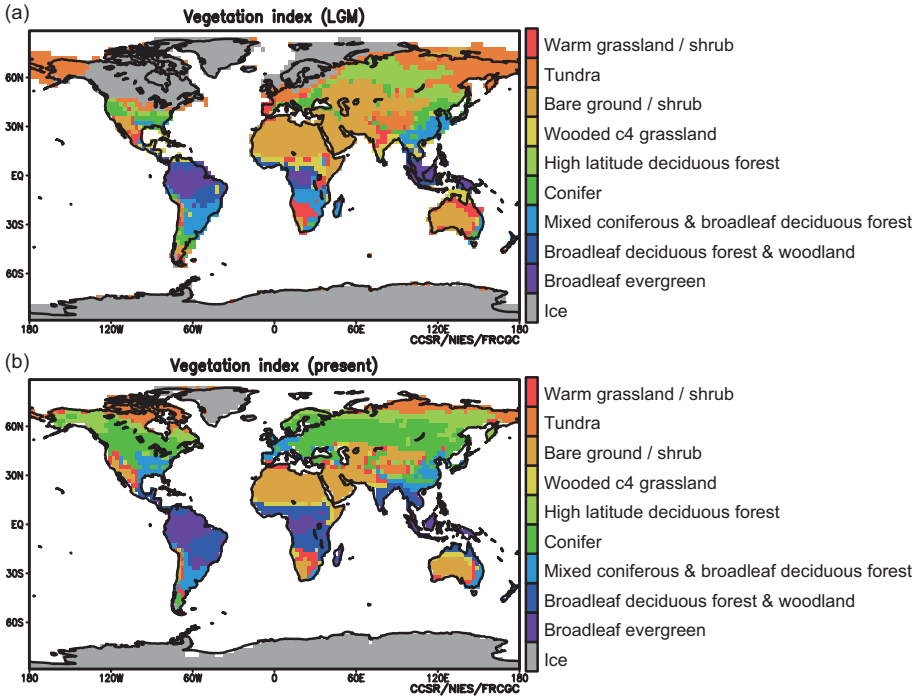

Fig. 1. Distributions of the vegetation in the **(a)** LGM and **(b)** PRE.

ACPD
8, 20463–20500, 2008

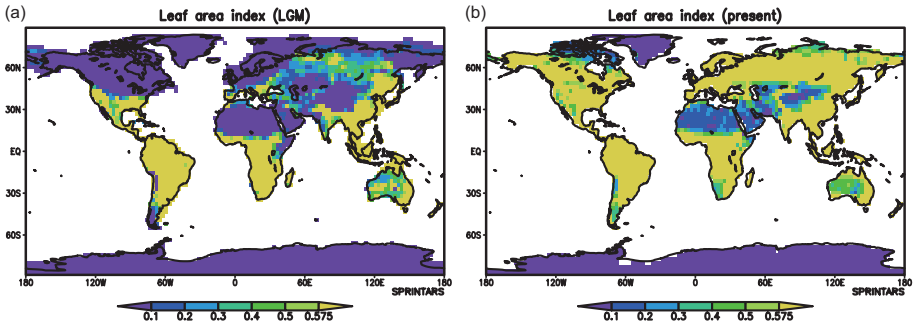

Fig. 2. Annual mean distributions of the leaf area index in the **(a)** LGM and **(b)** PRE.

ACPD
8, 20463–20500, 2008

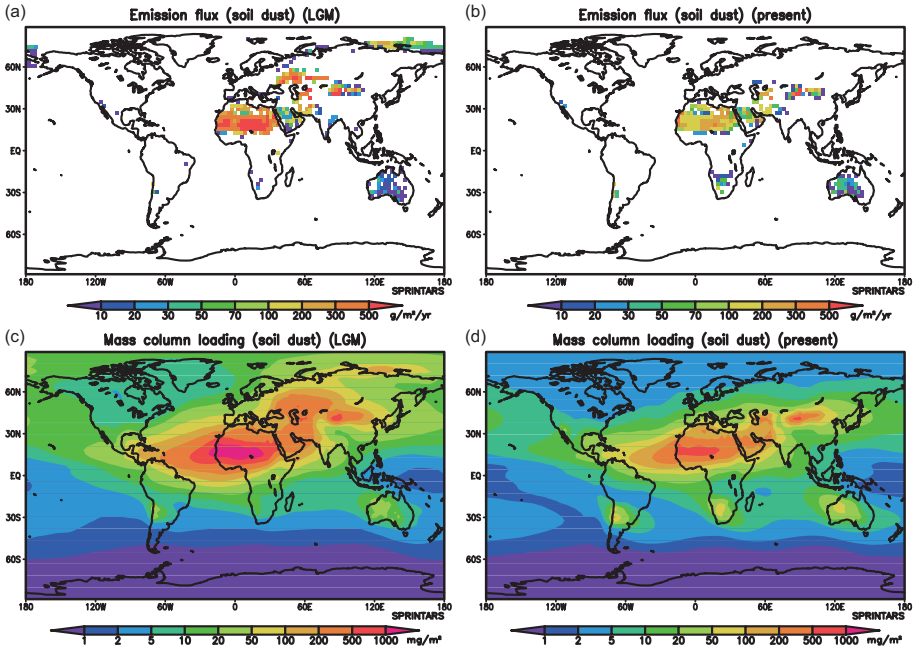

Fig. 3. Annual total distributions of the emission flux of soil dust aerosols in the **(a)** LGM and **(b)** PRE and annual mean distributions of the mass column loading of soil dust aerosols in the **(c)** LGM and **(d)** PRE.

ACPD
8, 20463–20500, 2008

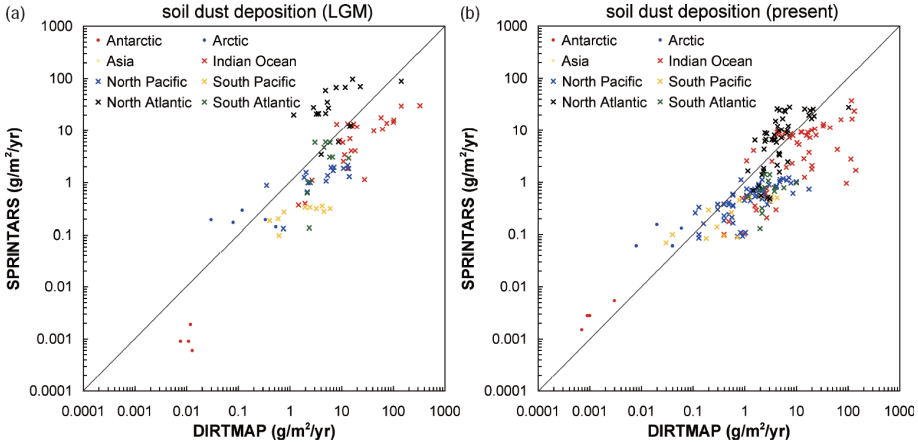

Fig. 4. Comparisons of annual total deposition flux of soil dust aerosols between the DIRTMAP database and SPRINTARS simulation in the **(a)** LGM and **(b)** PRE. Dots and crosses show comparisons with DIRTMAP from ice cores and marine sediments, respectively.

ACPD
8, 20463–20500, 2008

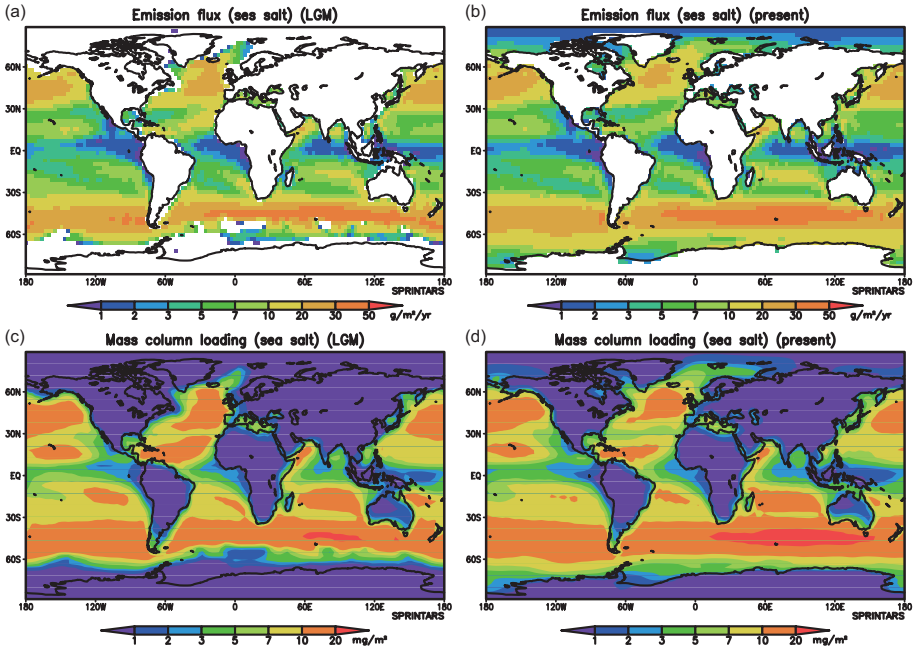

Fig. 5. Annual total distributions of the emission flux of sea salt aerosols in the **(a)** LGM and **(b)** PRE and annual mean distributions of the mass column loading of sea salt aerosols in the **(c)** LGM and **(d)** PRE.

ACPD
8, 20463–20500, 2008

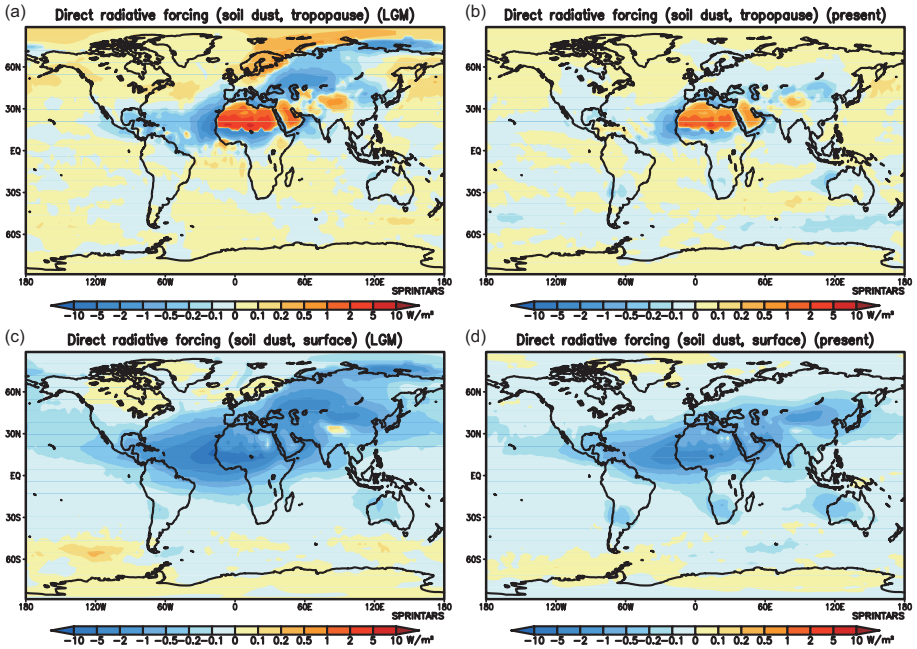

Fig. 6. Annual mean distributions of radiative forcing for the shortwave plus longwave radiation due to the direct effect of soil dust aerosols under the all-sky condition at the tropopause in the **(a)** LGM and **(b)** PRE and at the surface in the **(c)** LGM and **(d)** PRE.

ACPD
8, 20463–20500, 2008

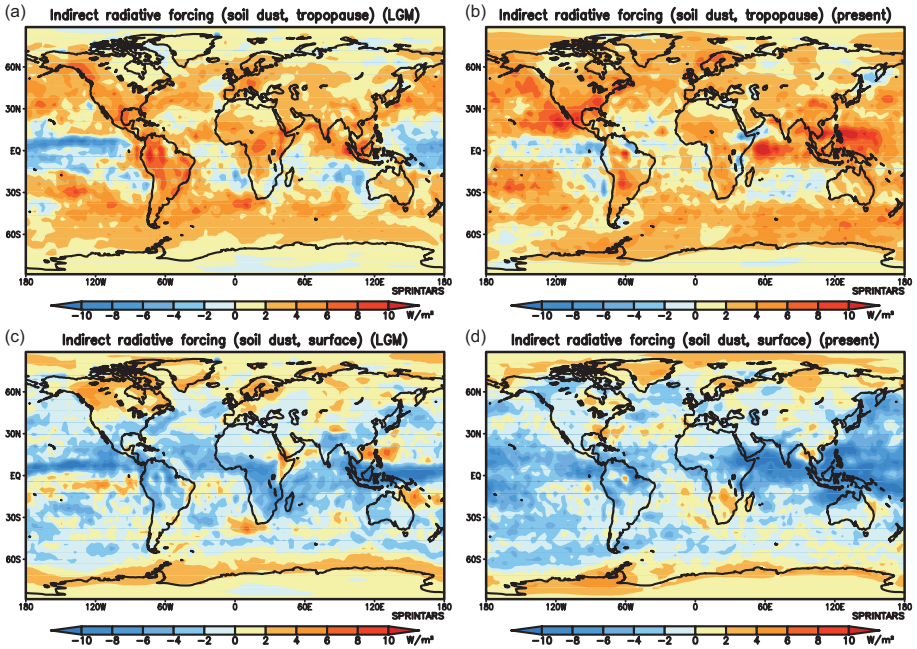

Fig. 7. Annual mean distributions of radiative forcing for the shortwave plus longwave radiation due to the indirect effect of soil dust aerosols at the tropopause in the **(a)** LGM and **(b)** PRE and at the surface in the **(c)** LGM and **(d)** PRE.

ACPD
8, 20463–20500, 2008